

Optical In Situ Micro Tribometer for Analysis of Real Contact Area for Contact Mechanics, Adhesion, and Sliding Experiments

Brandon A. Krick · Jennifer R. Vail ·
Bo N. J. Persson · W. Gregory Sawyer

Received: 1 July 2011 / Accepted: 26 September 2011 / Published online: 30 October 2011
© Springer Science+Business Media, LLC 2011

Abstract An instrument has been developed that allows in situ optical analysis and tribological measurements for contacts between solid bodies; an interferometric optical analysis can be used to measure and observe contact size, contact geometry, near contact topography, tribofilm formation, tribofilm motion, tribofilm thickness, wear debris formation, and wear debris morphology. The optical arrangement is in such a way that a 0th order interference fringe highlights the real contact area of contact, while near contact regions are height-mapped with higher order Newton's rings interference fringes. Images synchronized with force and position measurements allow for the potential to test and validate models for contact mechanics, adhesion, and sliding. The contact and friction measurement between a rough rubber sphere and a polished glass counterface were studied over a range of loads from 1 to 50 mN.

Keywords Contact area · In situ · Optical · Tribometer · Tribology · Contact mechanics · Rubber · Friction

1 Introduction

In situ tribometry is a powerful tool used by materials tribologists to study the interaction between surfaces during contact and sliding [1, 2]. There are various pathways

for in situ analysis of a surface. In situ spectroscopies such as Raman spectroscopy have been used to analyze the chemical nature of the interactions by examining the wear surface or transfer films during sliding or just after it exits the contact without changing the environment [3, 4]. In situ electron microscopy is increasingly popular; Varenberg used a scanning electron microscope to analyze the interaction at the interface from the side [5]. Marks showed a liquid-like transfer of gold with in situ transmission electron microscope experiments [6]. The state-of-the-art in in situ tribology was recently reviewed by Sawyer and Wahl [1, 2].

One phenomenon that has been historically probed with in situ techniques is the real area of contact between solids. In situ tribology and contact mechanics experiments are not entirely unprecedented, especially when examining the real contact area between solids [7–13]. Contact area has been indirectly monitored in situ by contact resistance measurements [8, 9] and optical methods of examining the contact through a transparent counter sample [7, 10–16]; Dyson and Hirst examined the real area of contact of metallic films with a phase contrast microscope through a glass disk [7]. Federle used in situ optical techniques to explore contact mechanics and adhesion in the feet of frogs, ants and other insects [14–16]. McCutchen examined the contact area between a polyvinyl chloride surface and an optically transparent counter surface using two optical methods: frustrated total internal reflection and optical interference of the Newton's rings type [10]. The Newton's rings interference can be used to measure contact because the destructive 0th order interference occurs at contact with higher order fringes radiating out in the near contact regions. The higher order fringes can also be used to map the near surface separations, and for closely spaced solids the distribution of interfacial separation, which is of crucial

B. A. Krick · J. R. Vail · B. N. J. Persson · W. G. Sawyer (✉)
Department of Mechanical and Aerospace Engineering,
University of Florida, Gainesville, FL 32611, USA
e-mail: wgsawyer@ufl.edu

B. N. J. Persson
IFF, FZ-Jülich, Jülich 52425, Germany

importance for topics such as sealing, mixed lubrication, and the contact heat resistance. These techniques have been used for in situ tribology experiments to explore both film thicknesses and contact geometries [10, 12, 13].

Here, we have designed and constructed a new instrument that uses microtribological probes and methods to perform indentation, friction, and wear experiments while making high fidelity optical interferometric measurements of the contact area. This instrument is capable of measuring normal and friction forces ranging from 10 μN to over 2 N. This design facilitates synchronized measurement of externally applied contact force (including adhesive), friction force, penetration depth, deformation, and in situ optical imaging of the contact with a spatial resolution limited by the diffraction limit. Preliminary optical in situ loading/unloading and sliding experiments were performed between a nitrile rubber half sphere and glass, with the aim to provide experimental measurements that can be compared to the available theories and models on contact area [8, 11, 17–29].

2 Description of the In Situ Optical Micro Tribometer

The in situ optical micro tribometer is capable of performing load/unload, friction, and wear experiments with in situ optical capabilities (Fig. 1). In an experiment, a sample is mounted directly to a load head; the load head measures both normal and frictional forces and is mounted to a piezoelectric stage that displaces the sample toward and away from a counter sample. Beneath the sample and counter sample is a microscope objective facing upward toward the sample; between the sample and objective is a transparent counter sample (in this case a flat optical window). The transparent counter sample is mounted to a piezoelectric stage that generates sliding between the samples. Figure 1 shows a schematic with important components.

A microscope objective (typically 5 \times or 10 \times) is mounted beneath the transparent counter sample. The objective has unique, low profile optical path to a 5 mega pixel Sony XCL-5005CR CCD camera. The sample is

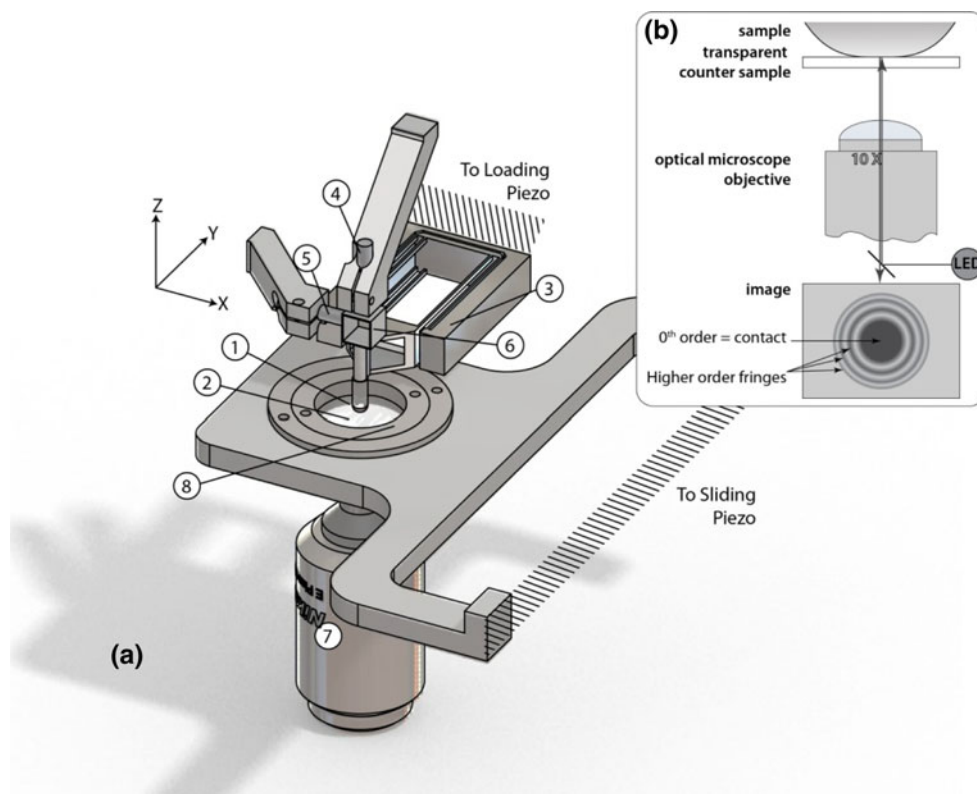


Fig. 1 **a** Schematic of optical in situ micro tribometer: the sample (1) is slid against a transparent counter sample (2). The sample is mounted directly to a calibrated cantilevered force transducer flexure (3). Capacitance probes (4 and 5) measure the displacement of a target (6) mounted on the cantilevered flexure; with the calibration of the flexure, these displacements provide the normal and friction forces. A microscope objective (7) mounted directly beneath the transparent counter sample held by a sample holder (8). **b** Schematic

of optical pathway. A monochromatic coherent light source passes through the microscope objective and up through the transparent counter sample. The light is reflected off of the surfaces of the sample and counter sample back through the microscope objective and ultimately to a CCD camera. In the image, there is a 0th order destructive interface representing contact and higher order fringes surrounding contact

illuminated through the objective with an interchangeable LED; for this experiment an LED of 595 nm with a measured FWHM of 16 nm was selected.

2.1 Imaging Methodology and Contact Area Analysis

When the sample is lowered into contact with the transparent counter sample a contact area may be observed through interference. At the most basic level, there is a destructive interference fringe of 0th order everywhere the samples are in contact with each other; this allows observation of contact area and geometry (Fig. 1b). In addition to the 0th order fringes, higher order fringes exist when the samples are separated; further information can be determined from the fringes, such as thickness of a film between the solids and relative distance between the solids. The fringe pattern oscillates from dark to light as the separation gap between the samples is increased. The separation distance required for destructive interference (Eq. 1) and constructive interference (Eq. 2) is a function of wavelength, λ , and order.

$$d_{\text{destructive}} = \frac{m}{2} \lambda \tag{1}$$

$$d_{\text{constructive}} = \frac{(2m + 1)}{4} \lambda \tag{2}$$

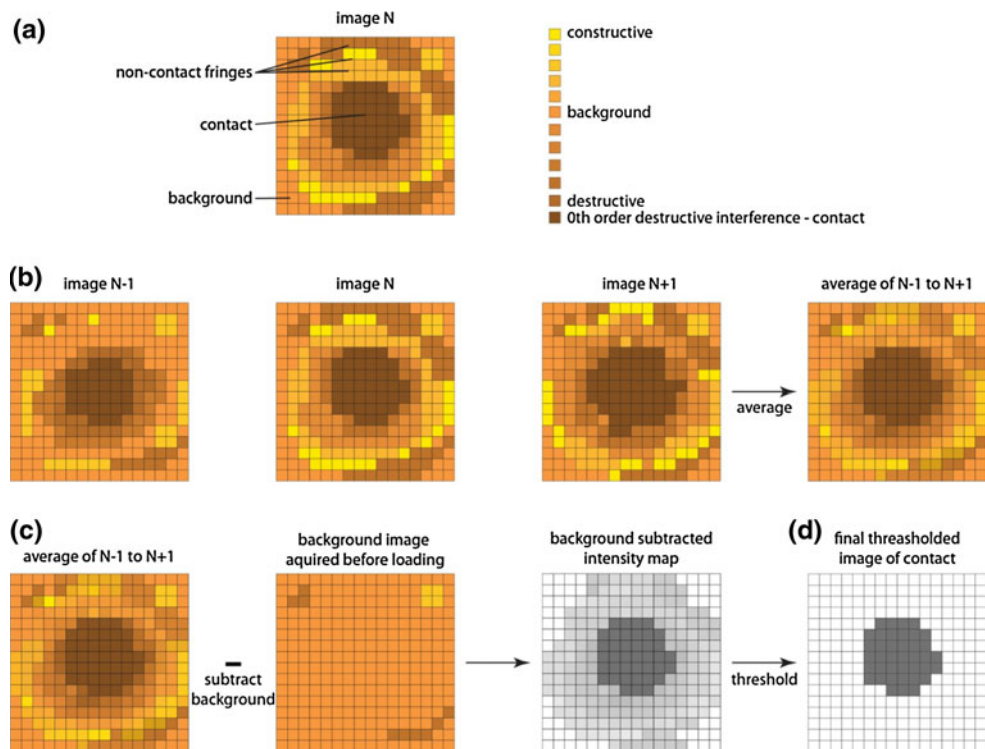
The optical fringe pattern phenomenon is caused by interference between light reflected from the interface

between the transparent counter sample and air and the π phase shifted light reflected off of the pin sample.

At a given magnification, the real contact area and geometry is given by the 0th order interference which manifests as a dark area on the digital image for these material sets. Thresholding techniques of the digital image can be applied to calculate this contact area. Unfortunately, additional features such as fringes surrounding the contact and impurities in the glass produce false contact spots in the analysis. To accommodate this error we apply a post processing technique illustrated in Fig. 2. The image that we are analyzing the contact area, image N, is an intensity profile with pixels correlating to contact spots, higher order fringes, background impurities, and a background level intensity (Fig. 2a). Contact is represented by the dark 0th order destructive interference. Surrounding the contact are constructive and destructive interference fringes and other features that are inherent impurities on the glass.

By simply applying a threshold to the image, one cannot accurately separate contact area from the background intensity because the higher order destructive fringes often produce false contact areas. To reduce this error, the image being analyzed is averaged with the image taken directly before and directly after the image of interest. Higher order, non-contact fringes will change as a result of a displacement of the rubber ball toward or away from the optical flat. If there is a change in the separation distance in the near contact zones, then the higher order fringes occupy

Fig. 2 Post processing technique schematic: **a** image N of contact at an applied load. Contact, represented by the dark 0th order destructive interference, is surrounded by constructive and destructive interference fringes and other features that are inherent impurities on the glass. **b** The image being analyzed, the previous image and the next image are averaged to preferentially weight contact and discount higher order fringes. **c** A background image acquired before loading began is subtracted from the averaged image. **d** A threshold is applied to the image revealing the contact area and geometry



different pixels from frame to frame. Consequentially, higher order dark fringes will not overlap throughout the three images as shown in Fig. 2b. This effectively removes higher order fringes, but does not remove impurities in the surface of the glass that result in false contact pixels.

Background impurities are removed by subtracting a background image acquired before loading from the averaged image (Fig. 2c). Finally a threshold can be applied to calculate the contact area (Fig. 2d). This contact area can be calculated by multiplying the number of pixels in contact by the square of the calibration constant $0.35 \mu\text{m}/\text{pixel}$. The accuracy of the reported contact area is limited by the diffraction limit of light and other optical effects in very thin separations.

2.2 Force Measurements and Positioning Metrology

The load head is responsible for holding the sample, measuring normal and tangential (friction) forces, and applying the normal load by bringing the sample into contact with the counter sample with a piezoelectric stage. It consists of a cantilever that is instrumented with two capacitance probes; one capacitance normal to the contact and one in the sliding direction.

The capacitive probes are aligned with a conductive target that is fixed to the end of the loading cantilever assembly. The probes are calibrated to monitor the change in distance between the capacitance probe and the target that is fixed to the cantilever. The cantilever assemblies consist of two double-leaf cantilevers that are mounted parallel to one another to constrain the flexures to rectilinear displacements. The use of a one double-leaf flexure would result in a change in slope at the capacitive target and would produce adverse effects [30]. The resolution of normal and tangential forces is only limited by the capacitance probe resolution and the stiffness of the interchangeable cantilevers.

Through cantilever selection, normal loads of 2 N or more can be applied for high load cantilevers and normal loads of less than $10 \mu\text{N}$ can be applied. This particular combination of cantilevers and of capacitive probes can measure forces with uncertainties better than $50 \mu\text{N}$ and resolution which exceed that by a factor of 10.

Piezoelectric stages are used for both loading displacements and sliding displacements. The piezoelectric stage responsible for bringing the sample into contact and modulating the normal load, the “loading piezo,” has a range of $100 \mu\text{m}$, resolution of 0.4 nm and repeatability of $\pm 1 \text{ nm}$. The piezoelectric stage that produces the sliding motion, the “lateral piezo,” has a range of $1,500 \mu\text{m}$, resolution of 3 nm and repeatability of $\pm 14 \text{ nm}$. All of the stages are operated under closed loop positioning control.

Experimental control and acquisition is achieved through LabView. All force and position measurement signals are conditioned externally and interface with LabView with 16 bit analog-to-digital acquisition and control. Force versus displacement measurements are typically taken at 1,000 samples per second. Images are also acquired with LabView and are time-synched with all force and position data at as quickly as 15 frames per seconds.

3 Materials

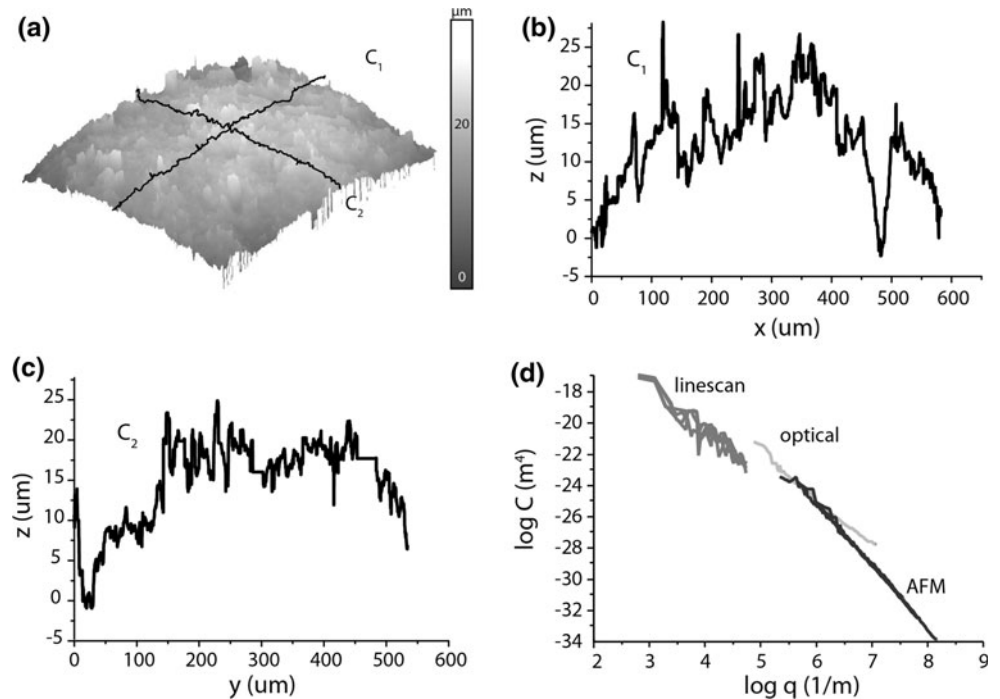
Commercially available Buna-N nitrile rubber spheres of 4.8 mm diameter were used in this study. The Buna-N rubber has a supplier specified durometer of 70A corresponding to a modulus of approximately 5.5 MPa. The spheres were cut in half with a razor blade and attached to the end of the cantilever. Prior to experiments, the half sphere was characterized with a Veeco Dektak 8 Advanced stylus profilometer, a Veeco Wyko NT9100 scanning white light interferometer (Fig. 3a–c), and an ASYLUM MFP-3D atomic force microscope; the measured RMS roughness of the rubber spheres was $5.2 \mu\text{m}$. The surface roughness power spectrum was determined from this characterization (Fig. 3d) [29] and the resulting fractal dimension is $D_f \sim 2$.

A borosilicate float glass optical window was used as the transparent counter sample. The windows were 25 mm in diameter and 3 mm thick. The manufacturer specified modulus of the glass is four orders of magnitude higher than the rubber sample at approximately 64 GPa. The glass samples have RMS roughness of 2.06 nm measured with the stylus profilometer; that is more than three orders of magnitude less than the roughness of the rubber. These large differences in roughness and modulus make the glass appear infinitely stiff and perfectly smooth when compared to the rubber sample.

4 Description of Loading and Sliding Experiments

For these experiments, a 2.4 mm radius nitrile rubber half sphere was pressed against and slid against borosilicate glass windows. The nitrile spherical cap was brought into contact with the glass window to a prescribed force; the piezo was commanded to move at a constant rate of $2.75 \mu\text{m}/\text{s}$ during loading and unloading. Four different experiments were run with target loads of 5, 10, 25, and 50 mN. Images were acquired at half second intervals and were synchronized with the experiments; these digital images were then processed to compute the measured real contact area.

Fig. 3 Surface profilometry of nitrile spherical cap 2.4 mm radius. **a** Surface profile acquired from a Veeco Wyko NT9100 Scanning White Light Interferometer. **b** and **c** line scans taken across sample indicated by C_1 and C_2 . **d** Surface roughness power spectrum of nitrile ball. The fractal exponent of the surface is 1.8; this determined by the slope of the $\log C$ versus $\log q$ relationship



Linear reciprocating sliding experiments were performed on the nitrile half sphere. For each test, the sample was brought into contact at the desired normal force loading: 25 and 50 mN; a static image was acquired before the onset of sliding. Sliding experiments were performed at sliding velocities of 20 and 50 $\mu\text{m/s}$ over a stroke of 800 μm ; images of the contact were acquired before and during sliding. Images were acquired at six frames per second.

5 Results and Discussion

Figure 4 shows the contact area as a function of externally applied normal load for nitrile rubber half spheres, where each data point represents a processed image file. There is a nearly linear increase in contact area with increasing force over the range of the experiments, as predicted by contact mechanics theories (see, e.g., Ref. [28]), as long as the area of contact, A , is small compared to the nominal contact area A_0 . This linearity means that the (average) pressure is the area of real contact is nearly constant.

In all cases, there is a strong hysteresis in the contact area plotted against externally applied force in the loading versus unloading of the rubber against the glass. This has been explained by considering the loading scenario as a crack closing between the rubber and the glass, and the unloading and breaking of contact as a crack opening: At a distance r away from the tip of a propagating crack the rubber experiences time-dependent deformation characterized by a frequency v/r , where v is the crack tip velocity.

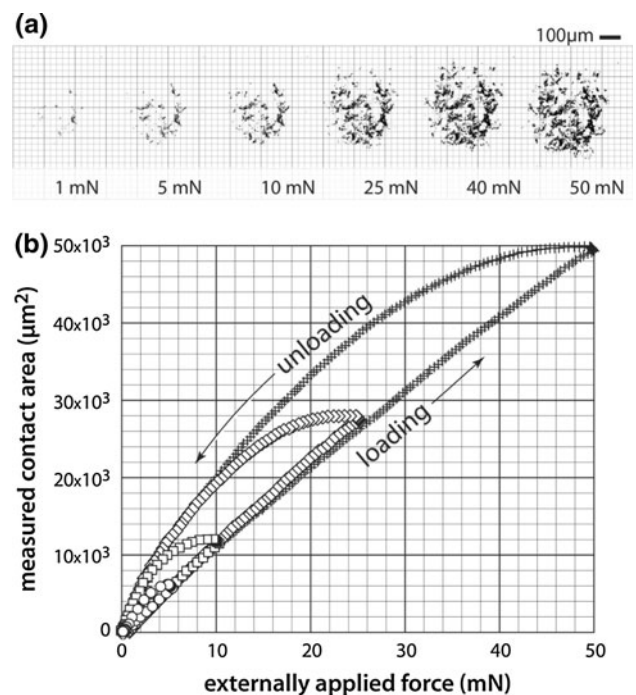


Fig. 4 Measured real contact area versus externally applied force of the nitrile spherical cap pressed against the borosilicate glass window. **a** Processed contact area images for loadings of 1, 5, 10, 25, 40, and 50 mN. **b** Contact area plotted against externally applied force for four loading and unloading profiles

Rubber-like materials are viscoelastic, and a large energy dissipation in the rubber may occur at a distance r from the crack tip where the perturbing frequency v/r is close to the frequency where $\tan \delta = \text{Im}E/\text{Re}E$ is maximal. For a fast

moving opening crack this may give rise to an effective interfacial energy $G = \gamma_0(1 + f(v))$, which may be enhanced by a factor of 100 or 1,000, while for a closing tip the interfacial energy may be reduced by a similar number (see Ref. [31, 32]). This is the origin of the strong hysteresis seen in our experiments.

The area and shape of the contact changes during sliding; the shear stress at the contact distorts the contact area and shears it in the direction of sliding. Figure 5 shows the contact geometry for the nitrile rubber for static and sliding conditions for loads of 25 and 50 mN and sliding velocities of 20 and 50 $\mu\text{m/s}$. At these loads and velocities, an increase in contact area is observed during sliding. This can be explained by the strong increase in the effective interfacial energy at the opening crack (at the exit of the contact region), see below. In this context, it is interesting to note that for silicone rubber, which can be considered as purely elastic with respect to the type of experiments discussed here, the opposite effect is observed, namely the static (or low sliding velocity) contact region is larger (and given by

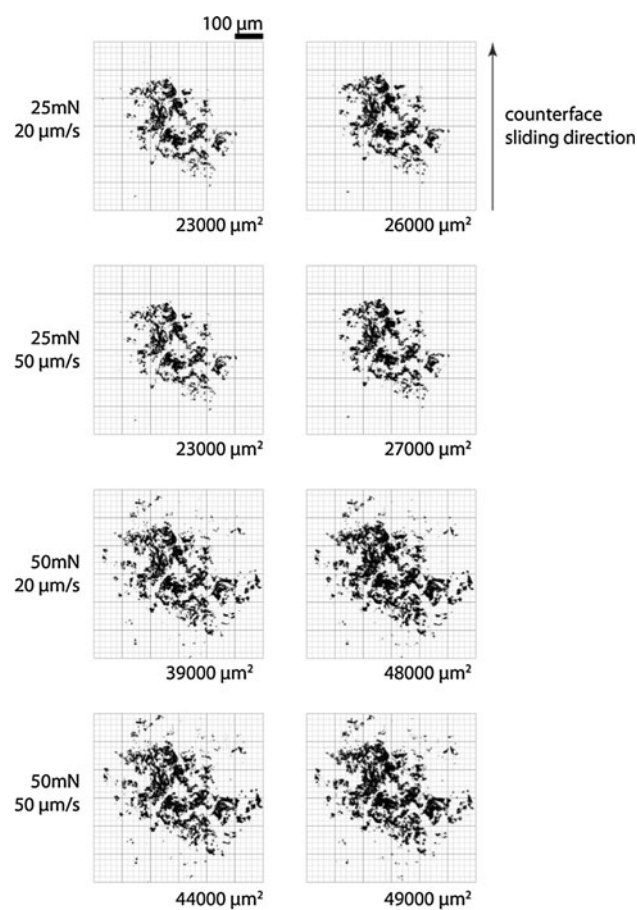


Fig. 5 Processed contact area images during static loading (*left*) and sliding (*right*) for loads of 25 and 50 mN and sliding speeds of 20 and 50 $\mu\text{m/s}$. There is a noticeable increase in contact area during steady state sliding

the JKR theory) than at higher velocities where the contact region is smaller and given accurately by the Hertz contact theory (e.g., negligible influence of adhesion) [33]. See also the discussion below.

The area of real contact depends, $A(\zeta)$ in general on the resolution ζ (or magnification) of the instrument used to study the system. This is illustrated in Fig. 6, which shows an elastic block (dotted area) in adhesive contact with a rigid rough substrate (dashed area). The substrate has roughness on many different length scales and the block makes partial contact with the substrate on all length scales. When a contact area is studied at low magnification, it appears as if complete contact occurs, but when the magnification is increased it is observed that in reality only partial contact has taken place. The true (or atomic) contact area $A(\zeta_1)$ is obtained at the highest magnification ζ_1 , corresponding to atomic resolution. The dependency of the area of contact, $A(\zeta)$, on the magnification ζ is of fundamental importance in many applications.

We have used the Persson contact mechanics theory [28, 34] to calculate the variation of the contact area with the magnification. In this theory, the surface roughness enters only via the surface roughness power spectrum $C(q)$. In Fig. 7, we show the logarithm (with 10 as the basis) of the surface power spectra as a function of the logarithm of the wave-vector, as obtained from AFM and line scan topography data (from Fig. 3) with a linear fit to the data corresponding to a root-mean-square roughness $h_{\text{rms}} = 6 \mu\text{m}$ and the fractal dimension $D_f = 2$ (or Hurst exponent $H = 1$). The fit curve corresponds to a surface with the

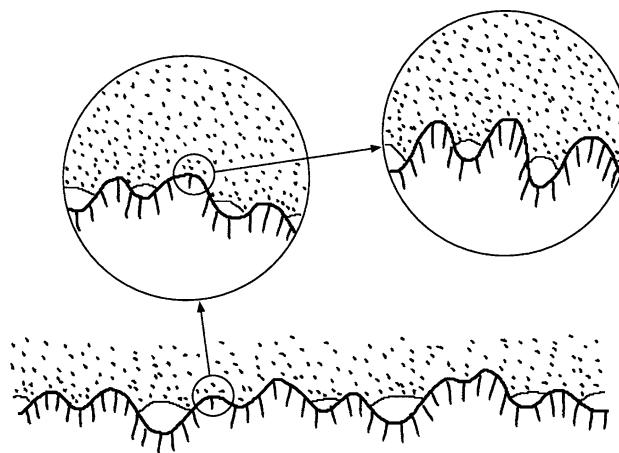


Fig. 6 An elastic block (dotted area) in adhesive contact with a rigid rough substrate (dashed area). The substrate has roughness on many different length scales and the block makes partial contact with the substrate on all length scales. When a contact area is studied, at low magnification it appears as if complete contact occurs, but when the magnification is increased it is observed that in reality only partial contact has taken place

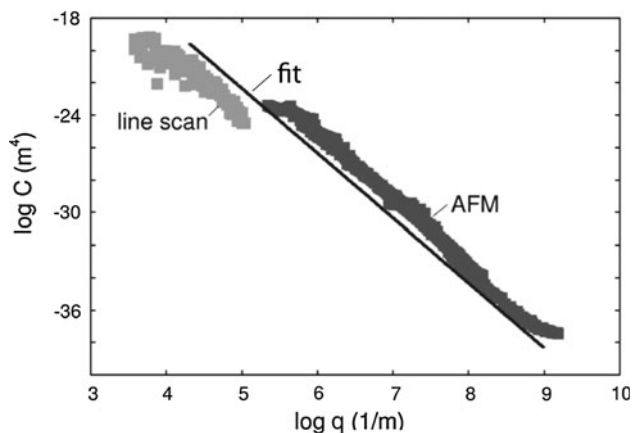


Fig. 7 The logarithm (with 10 as basis) of the surface power spectra as a function of the logarithm of the wave-vector. The plot contains AFM and line scan topography data, and a fit to the data corresponding to a root-mean-square roughness $h_{rms} = 6 \mu\text{m}$ and the fractal dimension $D_f = 2$ (or Hurst exponent $H = 1$). The fit corresponds to a surface with a root-mean-squared slope of 0.31 and surface area $A_{tot} = 1.14A_0$

root-mean-squared slope of 0.31 and the surface area $A_{tot} = 1.14A_0$ (where A_0 is the nominal (flat) surface area).

In Fig. 8, we show the calculated relative contact area A/A_0 (where A_0 is the nominal contact area) as a function of the logarithm (with 10 as basis) of the magnification for models both with and without adhesion [34] and the without adhesion [28]. In the calculation, we have assumed the power spectra given by the fit line in Fig. 7 (with $q_0 < q < q_1$, $q_0 = 2 \times 10^4 \text{ m}^{-1}$, $q_1 = 10^9 \text{ m}^{-1}$), and the rubber elastic modulus $E = 5 \text{ MPa}$ and squeezing pressure $p = 0.6 \text{ MPa}$. The curve denoted “adhesion” is calculated using the theory of Ref. [34] assuming the work of adhesion $\gamma_0 = 0.08 \text{ J/m}^2$.

The resolution of the optical instrument we have used to study the contact between the rubber ball and the flat glass surface is of order $\lambda \approx 1 \mu\text{m}$, which corresponds to the magnification $\zeta \approx (\pi/\lambda)/q_0 \approx 100$. According to our calculations (see Fig. 8) at this magnification, adhesion already manifests itself and increasing the magnification even more does not decrease the contact area. That is, at length scales shorter than $\approx 1/(10q_0)$ (see Fig. 8) the adhesion pulls the surfaces into complete contact so that increasing the magnification above 10 does not result in a decrease in the contact area as would be the case without adhesion (in Fig. 8).

The contact pressure we use in the calculations is similar to what prevail in the central region of the contact pictures in Fig. 4: the load $F_N = 50 \text{ mN}$ is mainly distributed over a nominal contact area of $300 \times 300 \mu\text{m}^2$ giving an average pressure of order $p = 0.6 \text{ MPa}$ in the central part of the contact region. In this region, the relative contact area A/A_0 is of order 0.5, which is similar to what we observe in our calculation, see Fig. 8.

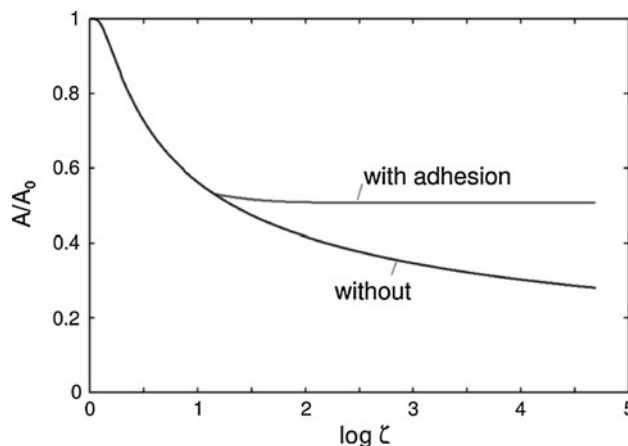


Fig. 8 The calculated relative contact area A/A_0 (where A_0 is the nominal contact area) as a function of the logarithm (with 10 as basis) of the magnification for models both with and without adhesion. In the calculation, we have assumed the power spectra from Fig. 7 (curve with $q_0 < q < q_1$, $q_0 = 2 \times 10^4 \text{ m}^{-1}$, $q_1 = 10^9 \text{ m}^{-1}$), and the rubber elastic modulus $E = 5 \text{ MPa}$ and squeezing pressure $p = 0.6 \text{ MPa}$. The curve denoted “adhesion” is calculated using the theory of Ref. [34] assuming the work of adhesion $\gamma_0 = 0.08 \text{ J/m}^2$

When surface roughness occurs, in order for two solids to make adhesive contact, the surfaces must bend at the interface. This will result in (asperity induced) elastic energy stored at the interface which is, at least in part, given back during pull-off and helps to break the interfacial bond. This effect is described by the effective interfacial binding energy (see Ref. [34]) $\gamma_{eff}(\zeta)A_0 = \gamma_0 A(\zeta_1) - U_{e1}(\zeta)$ where $U_{e1}(\zeta)$ is the elastic energy stored within the interface including only the roughnesses with wave-vector $q > q_0\zeta$. In Fig. 9, we show the calculated effective interfacial energy γ_{eff} (in units of the interfacial energy γ_0 for flat surfaces) as a function of the logarithm (with 10 as basis) of the magnification. The curve with adhesion is calculated assuming the work of adhesion $\gamma_0 = 0.08 \text{ J/m}^2$. Note that γ_{eff} (1) vanishes. This implies that the area of real contact will be proportional to the squeezing force even when adhesion is included [39]. This is illustrated in Fig. 10 which shows the calculated relative contact area A/A_0 (where A_0 is the nominal contact area), at the highest magnification, as a function of the applied pressure. Note that the area of real contact varies (nearly) linearly with the pressure or load even when adhesion is included, which is in good agreement with the experimental data shown in Fig. 4 during loading. During unloading this is no longer the case, because of the strong increase in the effective interfacial binding energy $\gamma_0 \rightarrow G = \gamma_0 (1 + f(v))$ at the opening crack during unloading, see below.

The area and shape of the contact changes during sliding; the shear stress at the contact distorts the contact area and shears it in the direction of sliding. Figure 5 shows the contact area and geometry for the nitrile rubber for static

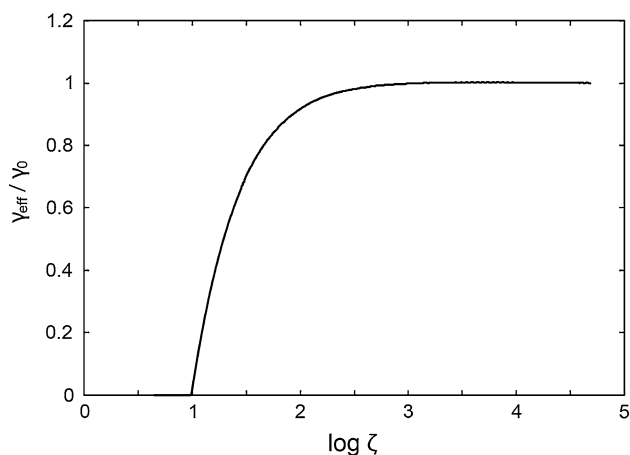


Fig. 9 The calculated effective interfacial energy γ_{eff} (in units of the interfacial energy γ_0 for flat surfaces) as function of the logarithm (with 10 as basis) of the magnification. In the calculation, we have assumed the power spectra from Fig. 7, an elastic modulus of $E = 5$ MPa, and the work of adhesion $\gamma_0 = 0.08$ J/m²

and sliding conditions for loads of 25 and 50 mN and sliding velocities of 20 and 50 $\mu\text{m/s}$. At these loads and velocities, an increase in contact area is observed. When a rubber ball with smooth surface is sliding on a hard smooth substrate, or a hard smooth ball on a flat rubber surface, the area of real contact usually decreases with increasing velocity, roughly from the JKR (adhesive) theory limit for zero velocity to the Hertz (non-adhesive) limit for high enough velocity [33, 35–37]. This is usually attributed to the build-up of elastic deformation energy, due to the frictional shear stress at the sliding interface, which may reduce the adhesional interaction in a very similar way as the asperity-induced elastic energy reduce the adhesion on

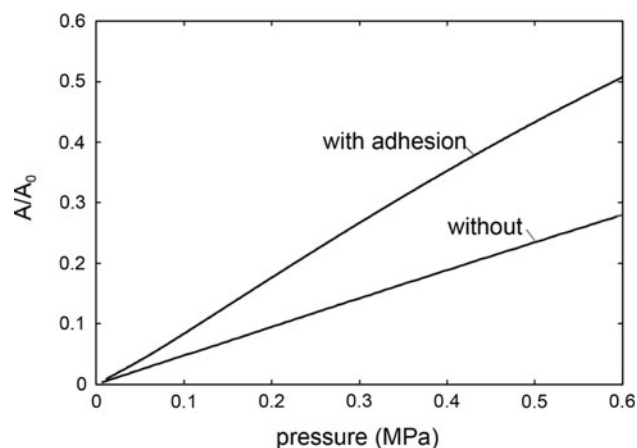


Fig. 10 The calculated relative contact area A/A_0 (where A_0 is the nominal contact area), at the highest magnification, as a function of the applied pressure for the cases of both with and without adhesion. In the calculation, we have assumed the power spectra from Fig. 2, and the rubber elastic modulus $E = 5$ MPa. The curve with adhesion is calculated assuming the work of adhesion $\gamma_0 = 0.08$ J/m²

rough surfaces. Thus, during sliding elastic energy is “stored” at the interface, which helps to break the adhesive bonds, making the contact essentially non-adhesive at high enough velocity (this assumes that the rubber friction force increases with increasing sliding velocity). One such mechanism was studied by Savkoor et al. [38], and another in Ref. [39] where it was also shown that the quantitative theory to describe the observed effects may still be lacking.

There exist a second mechanism, which tends to increase the contact area, and which may be particular important in our applications. To explain this, note first that the theory of adhesive bonding can be formulated as a theory of interfacial cracks. During sliding, the line boundary between contact and non-contact will consist of closing cracks on the front side, and an opening crack on the exit side of the sliding ball. For viscoelastic materials such as rubber there may be a strong enhancement in the effective interfacial energy at opening cracks [32, 40] which effectively may increase the adhesive interaction and the contact area. This effect is particular important for a rubber with a high glass transition temperature, which behave highly dissipative already for relative low perturbing frequencies (or low sliding velocities). On the contrary, rubber with low glass transition temperature may behave as a nearly perfect elastic material with respect to the perturbing frequencies involved in sliding at low velocities. We illustrate this in Fig. 11 which shows the calculated (using the theory presented in Ref. [32]) effective interfacial crack propagation energy as a function of the crack tip speed for PDMS and bromobutyl rubber (filled). Unfortunately, we do not have the viscoelastic modulus for nitrile rubber, which enter in the calculation of γ_{eff} , but the glass transition temperature of nitrile rubber

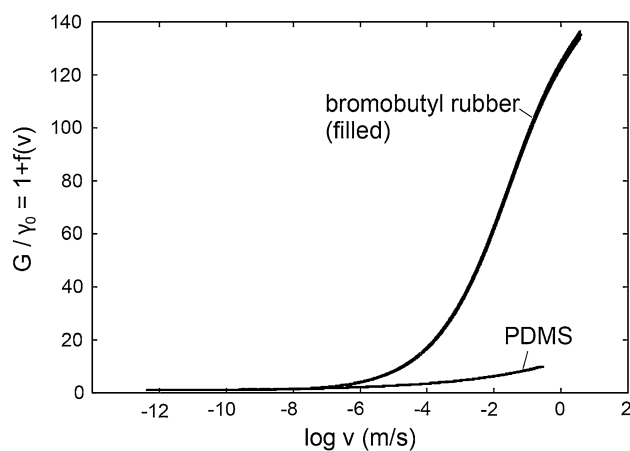


Fig. 11 The calculated effective interfacial crack propagation energy as a function of the crack tip speed for PDMS and bromobutyl rubber (filled). PDMS has a much lower glass transition temperature and bromobutyl rubber and much higher crack tip velocities are necessary for G to reach its high-velocity plateau value

($T_g \approx -26$ °C) is much higher than that of bromobutyl rubber ($T_g \approx -73$ °C), which will result in even larger γ_{eff} in the studied velocity range. PDMS has a much lower glass transition temperature ($T_g \approx -120$ °C) than bromobutyl rubber, and much higher crack tip velocities are necessary for γ_{eff} to reach its high-velocity plateau value [31, 32].

The fact that in most cases the contact area decreases rather than increases indicate that in most cases the first effect discussed above, involving the elastic energy “stored” at the interface, may in most cases be the most important one for smooth surfaces. However, the opening crack propagation mechanism is proportional to the length L of the boundary line between contact and non-contact. For smooth surfaces, this length scales linearly with the diameter D of the contact area. Since the area scale as $A \approx D^2$, we have $L \approx A/D$. Now assume that (at least) one of the solids has surface roughness. In this case, the contact area may consist of a large number, say N , of small contact spots (see Fig. 4). If d is the typical diameter of a contact spot and A is the total contact area, then $N \approx A/d^2$ and the total length of the region between contact and non-contact (crack tip line) becomes $L \approx Nd \approx A/d \gg A/D$. Thus, surface roughness may strongly enhance the contribution from the opening crack to the change in the contact area with increasing sliding velocity. We believe this is the explanation for why we observe an increase in the contact area for our sliding system. We also note that nitrile butadiene rubber (which has much higher glass transition temperature than bromobutyl rubber), is much more dissipative at low frequency than silicon rubber used in most of the earlier studies. This too will tend to enhance the importance of the opening crack mechanism in our case, as compared to most of the earlier studies.

Finally, let us note that there is a fundamental difference between having the roughness on the rubber side or on the hard counter surface. If a rubber block (e.g., a ball) is sliding on a hard rough substrate the surface asperities will exert pulsating deformations on the rubber surface which will lead to energy dissipation via the internal friction of the rubber [28]. Thus, in this case the roughness asperities will contribute to the observed friction. In addition, at high sliding velocity the contact area may decrease as the rubber is elastically stiffer when exposed to high frequency perturbations as compared to a static stress field. (Note: at very high sliding speed the frictional heating may make the rubber softer and result in an increase in the contact area.). On the other hand, if the hard surface is perfectly flat, and the rubber surface rough, then during sliding of the rubber block on the substrate the same rubber asperities will be in contact with the substrate the whole time. In this case, assuming steady sliding, no asperity-induced bulk energy dissipation will exist [41].

6 Conclusions

An in situ optical micro tribometer has been developed to explore the contact between two solids in intimate contact during loading and sliding. The instrument has been shown to successfully measure normal and tangential forces with uncertainties of better than 50 μN . Dimensional positioning of the samples can be resolved to 0.4 nm in the z direction and 14 nm in the sliding direction. The interferometric technique can resolve nanometers of separation, but is limited spatially to characteristic wavelengths of light due to diffraction, but the coherence of the LED gives over 10 μm of separation through which to capture fringes. With this instrument, real area of contact can be explored and the topography of the near contact region can be accurately measured.

Experiments have been completed in an effort to elucidate the contact behavior of a rough rubber half sphere when pressed against and slid against a smooth borosilicate glass window. A strong hysteresis in loading/unloading was observed in the contact area versus force. Sliding introduced a distortion in the contact geometry and an increase in contact area for the nitrile half sphere when slid on glass at loads of 25 and 50 mN and sliding velocities of 20 and 50 $\mu\text{m/s}$.

Acknowledgments The authors gratefully acknowledge Bertrand Bellaton at CSM instruments for collaboration and development of a low profile optical path for the objective, camera, and light source. We would also like to thank David Hahn, Dan Dickrell, Pete Dillinger, and Nicolas Argibay at the University of Florida and Nestor Rodriguez and Paolo Mangiagalli at Becton–Dickinson for useful discussion and collaboration.

References

1. Sawyer, W.G., Wahl, K.J.: Accessing inaccessible interfaces: in situ approaches to materials tribology. *MRS Bull.* **33**, 1145–1148 (2008)
2. Wahl, K.J., Sawyer, W.G.: Observing interfacial sliding processes in solid–solid contacts. *MRS Bull.* **33**, 1159–1167 (2008)
3. Scharf, T.W., Singer, I.L.: Monitoring transfer films and friction instabilities with in situ Raman tribometry. *Tribol. Lett.* **14**, 3–8 (2003)
4. Rebelo de Figueiredo, M., Muratore, C., Franz, R., Chromik, R., Wahl, K., Voevodin, A., O’Sullivan, M., Lechthaler, M., Mitterer, C.: In situ studies of tic1 – nrx hard coating tribology. *Tribol. Lett.* **40**, 365–373 (2010)
5. Murarash, B., Varenberg, M.: Tribometer for in situ scanning electron microscopy of microstructured contacts. *Tribol. Lett.* **41**, 319–323 (2011)
6. Merkle, A.P., Marks, L.D.: Liquid-like tribology of gold studied by in situ tem. *Wear* **265**, 1864–1869 (2008)
7. Dyson, J., Hirst, W.: The true contact area between solids. *Proc. Phys. Soc. Lond. Sect. B* **67**, 309–312 (1954)
8. Bowden, F.P., Tabor, D.: *The Friction and Lubrication of Solids*. Oxford University Press, Oxford (1954)

9. Holm, R.: *Electric Contacts Handbook*. Springer-Verlag, Berlin (1958)
10. Mccutchen, C.W.: Optical systems for observing surface topography by frustrated total internal reflection and interference. *Rev. Sci. Instrum.* **35**, 1340–1345 (1964)
11. O'Callaghan, P.W., Probert, S.D.: Prediction and measurement of true areas of contact between solids. *Wear* **120**, 29–49 (1987)
12. Chromik, R.R., Baker, C.C., Voevodin, A.A., Wahl, K.J.: In situ tribometry of solid lubricant nanocomposite coatings. *Wear* **262**, 1239–1252 (2007)
13. Wahl, K.J., Chromik, R.R., Lee, G.Y.: Quantitative in situ measurement of transfer film thickness by a Newton's rings method. *Wear* **264**, 731–736 (2008)
14. Federle, W., Barnes, W.J.P., Baumgartner, W., Drechsler, P., Smith, J.M.: Wet but not slippery: boundary friction in tree frog adhesive toe pads. *J. R. Soc. Interface* **3**, 689–697 (2006)
15. Federle, W., Endlein, T.: Locomotion and adhesion: dynamic control of adhesive surface contact in ants. *Arthropod Struct. Dev.* **33**, 67–75 (2004)
16. Federle, W., Riehle, M., Curtis, A.S.G., Full, R.J.: An integrative study of insect adhesion: mechanics and wet adhesion of pretarsal pads in ants. *Integr. Comp. Biol.* **42**, 1100–1106 (2002)
17. Bowden, F.P., Tabor, D.: The area of contact between stationary and between moving surfaces. *Proc. R. Soc. Lond. Ser. A* **169**, 391–413 (1939)
18. Archard, J.F.: Elastic deformation and the laws of friction. *Proc. R. Soc. Lond. Ser. A* **243**, 190–205 (1957)
19. Greenwood, J.A., Williamson, J.B.P.: Contact of nominally flat surfaces. *Proc. R. Soc. Lond. Ser. A* **295**, 300–319 (1966)
20. Whitehouse, D.J., Archard, J.F.: The properties of random surfaces of significance in their contact. *Proc. R. Soc. Lond. Ser. A* **316**, 97–121 (1970)
21. Johnson, K.L., Kendall, K., Roberts, A.D.: Surface energy and the contact of elastic solids. *Proc. R. Soc. Lond. Ser. A* **324**, 301–313 (1971)
22. Kendall, K.J.: Adhesion and surface energy of elastic solids. *J. Phys. D* **4**, 1186–1195 (1971)
23. Derjaguin, B.V., Muller, V.M., Toporov, Y.P.: Effect of contact deformations on the adhesion of particles. *J. Colloid Interface Sci.* **53**, 314–326 (1975)
24. Tabor, D.: Surface forces and surface interactions. *J. Colloid Interface Sci.* **58**, 2–13 (1977)
25. Maugis, D.: Adhesion of spheres: The jkr-dmt transition using a dugdale model. *J. Colloid Interface Sci.* **150**, 243–269 (1992)
26. Greenwood, J.A.: Adhesion of elastic spheres. *Proc. Math. Phys. Eng. Sci.* **453**, 1277–1297 (1997)
27. Johnson, K.L.: Mechanics of adhesion. *Tribol. Int.* **31**, 413–418 (1998)
28. Persson, B.N.J.: Theory of rubber friction and contact mechanics. *J. Chem. Phys.* **115**, 3840–3861 (2001)
29. Persson, B.N.J.: Contact mechanics for randomly rough surfaces. *Surf. Sci. Rep.* **61**, 201–227 (2006)
30. Varenberg, M., Peressadko, A., Gorb, S., Arzt, E., Mrotzek, S.: Advanced testing of adhesion and friction with a microtribometer. *Rev. Sci. Instrum.* **77**, 066105 (2006)
31. Persson, B.N.J., Albohr, O., Heinrich, G., Ueba, H.: Crack propagation in rubber-like materials. *J. Phys. Condens. Matter* **17**, R1071–R1142 (2005)
32. Persson, B.N.J., Brener, E.A.: Crack propagation in viscoelastic solids. *Phys. Rev. E* **71**, 036123 (2005)
33. Vorvolakos, K., Chaudhury, M.K.: The effects of molecular weight and temperature on the kinetic friction of silicone rubbers. *Langmuir* **19**, 6778–6787 (2003)
34. Persson, B.N.J.: Adhesion between an elastic body and a randomly rough hard surface. *Eur. Phys. J. E* **8**, 385–401 (2002)
35. Barquins, M., Roberts, A.D.: Rubber-friction variation with rate and temperature—some new observations. *J. Phys. D* **19**, 547–563 (1986)
36. Chateauminois, A., Danh, T.N., Paolino, P., Audry, M.C., Fretigny, C., Le Chenadec, Y., Portigliatti, M., Barthel, E.: Surface pressure and shear stress fields within a frictional contact on rubber. *J. Adhes.* **87**, 235–250 (2011)
37. Wu-Bavouzet, F., Clain-Burckbuchler, J., Buguin, A., De Gennes, P.G., Brochard-Wyart, F.: Stick-slip: wet versus dry. *J. Adhes.* **83**, 761–784 (2007)
38. Savkoor, A.R., Briggs, G.A.D.: Effect of tangential force on contact of elastic solids in adhesion. *Proc. R. Soc. Lond. Ser. A* **356**, 103–114 (1977)
39. Persson, B.N.J., Sivebaek, I.M., Samoilo, V.N., Zhao, K., Volokitin, A.I., Zhang, Z.: On the origin of Amonton's friction law. *J. Phys. Condens. Matter* **20**, 395006 (2008)
40. Carbone, G., Mangialardi, L.: Adhesion and friction of an elastic half-space in contact with a slightly wavy rigid surface. *J. Mech. Phys. Solids* **52**, 1267–1287 (2004)
41. Persson, B.N.J., Volokitin, A.I.: Rubber friction on smooth surfaces. *Eur. Phys. J. E* **21**, 69–80 (2006)